Engineering Journal issn: 0125-8281

Article

Compressive Behaviors of Hydrophobic Sheets Using Finite Element Analysis

Tumrong Puttapitukporn[a,*] **and Parawat Songpunnateegul**[b]

Department of Mechanical Engineering, Faculty of Engineering, Kasetsart University, Bangkok 10900, Thailand
E-mail: [a]fengtop@ku.ac.th (Corresponding author), [b]Parawat.so@ku.th

Abstract. Thai Microelectronics Centre (TMEC) used soft lithography techniques to fabricate hydrophobic sheets made of PDMS material for various micropillar patterns. The F8 and F13 micropatterns had high water contact angle and resisted high compressive load on top of hydrophobic sheets [17]. This research aimed to reinvestigate for truly understanding compressive behavior of these micropillar patterns under compressive loading. The finite element models of F8 and F13 micropatterns were constructed in Ansys APDL 2019R3 software. The accurate material model for PDMS under compressive loading was Ogden 3rd parameter material model as discussed in [13]. We introduce a novel mathematical technique implemented in MATLAB R2021a software. This technique aims to ascertain material constants and their associated stability regions. While the proposed method for determining material constants is deemed innovative and intriguing. Finally, uniform compressive load as a function of vertical deformation was found for each micropillar pattern. We found that load-deflection curves were stiffer than previous study discussed in [17] since we had no strain limit range in our study. Finally, the maximum uniform compressive loads, before the initial collapse of micropillar patterns, were 34.334 kPa and 16.694 kPa for F8 and F13 micropatterns respectively.

Keywords: Micropillar, Ogden material model, PDMS, modified PP algorithm, Ansys, MATLAB, hydrophobic sheet.

ENGINEERING JOURNAL Volume 28 Issue 6
Received 12 June 2023
Accepted 31 May 2024
Published 30 June 2024
Online at https://engj.org/
DOI:10.4186/ej.2024.28.6.25

DOI:10.4186/ej.2024.28.6.25

1. Introduction

Micro-structured surfaces are widely used in various medical areas and marine constructions because of their hydrophobic properties, which inhibit the formation of algae stains, germs, and barnacles on maritime structures [1]. Effective improvements of hydrophobic properties on surfaces are to fabricate them from low surface energy materials and to create high surface roughness which is accomplished by micropillar-like structures. Currently, extensive research has focused on fabrication of hydrophobic sheets made from PDMS materials and studying of mechanical behaviors of these hydrophobic surfaces via mathematical formulations or finite element methods. It is costly to fabricate hydrophobic sheets which are not only the cost of low surface energy materials but also facilities to cultivate micropillar-like structures. Rahmawan et al. [2] studied strength of the shear adhesion found on PUA micropillar arrays (5 μm diameter) of different aspect ratios and spacing ratios which were fabricated by replica molding from the PDMS mold. They found that the strength of the shear adhesion was improved by covering each micropillar with silica particles. Kim et al. [3] presented fabrication of tapered silicon pillar templates and their replication into LDPE thermoplastic. Moreover, micropillar tapering angles were studied for optimal friction performance. They found that as tapering angle decreased, deformation was more pronounced throughout the entire pillar. Mohamed et al. [4] reviewed cutting-edge technologies on fabrication, application, and stability of superhydrophobic surfaces. Oyunbaatar et al. [5] fabricated PDMS pillars with microgrooves used for biomechanical characterization of cardiomyocyte. The PDMS micropillar arrays with microgrooves were fabricated using a unique micro-mold made using SU-8 double layer processes. Sabbah, Youssef and Damman [6] had built micro-wrinkling patterns to introduce surface roughness onto PDMS sheets for studying of the water contact angles, WCA. They found that for smooth PDMS surface, WCA was 110 ^{o}; however, with micro-wrinkling patterns, WCA could be up to 180^{o}. Atthi et al. [7] fabricated various biomimetic antifouling surfaces made from PDMS by using the soft lithographic technique on silicon substrate. They discovered that the C-RESS pattern has the highest durability with the smallest suppression of the WCA after a scratch test of 1.3°. The adhesion of barnacle and algae on the C-RESS pattern is significantly reduced compared to other patterns. Li et al. [8] studied fabrication and nanoindentation characterization of nickel micro-pillar mold for nanoimprint lithography. These micropatterned metal sheets combine good strength and ductility, flexibility, and workability.

Hyperelastic materials are frequently used in fabrication of hydrophobic surfaces in which their material properties are governed by constitutive equations. Kim and Jeong [9] studied measurement of ~~n~~onlinear mechanical properties of surfactant-added PDMS. Three nonlinear mechanical models like a Neo–Hookean, Mooney–Rivlin, and Ogden were computed from the experimentally measured stress–strain data. The Ogden model for the surfactant-added PDMS showed good agreement with the experimental data. In the case of the Neo–Hookean and Mooney–Rivlin models, they could be preferable for the structural analysis of the micro device with the surfactant-added PDMS in the small strain region. Shahzad et al. [10] aimed to characterize hyperelastic material and to determine a suitable strain energy function (SEF) for an indigenously developed rubber to be used in flexible joint use for thrust vectoring of solid rocket motor. To evaluate appropriate SEF uniaxial and volumetric tests along with equi-biaxial and planar shear tests were conducted. Digital image correlation (DIC) technique was utilized to have strain measurements for biaxial and planar specimens to input stress-strain data in Abaqus. Yeoh model was the right choice, among the available material models, because of its ability to match experimental stress-strain data at small and large strain values. Ribeiro et al. [11] studied constitutive models of PDMS material using biaxial test. Numerical studies were also carried out using the most popular constitutive models, namely Mooney-Rivlin, Yeoh and Ogden, for comparison with the experimental measurements. The numerical simulations with the Yeoh model presented the most accurate results for PDMS behavior. Thanakhun and Puttapitukporn [12] studied PDMS material models for anti-fouling surfaces used for finite element method. The accuracies of the PDMS material models, which were the Neo-Hookean, Mooney-Rivlin 3 and 5 parameters, Ogden (1st, 2nd, 3rd order), Yeoh (1st, 2nd, 3rd order) and Arruda-Boyce material models, were evaluated and compared to experimental data from uniaxial tensile test and punch-shear test. They found that the most accurate material model to simulate both the uniaxial tension and shear loading was the Yeoh 3rd order material model; however, these accuracies would be valid for small strain range. Phothiphatcha and Puttapitukporn [13] proposed the PP algorithm, a MATLAB code, used for determining material constants and their associated stability strain range of hyperelastic materials. Their constitutive models comprised of Neo-Hookean; 3, 5, and 9 parameters, Mooney-Rivlin; 2nd and 3rd order Yeoh; and 1st, 2nd, and 3rd order Ogden. Then, they evaluated accuracy of their material constants obtained from uniaxial test data for PDMS material with results obtained from ANSYS APDL software and found that PP algorithm produced a lower RSS. Finally, the Ogden 3rd order model was the accurate constitutive model for compressive test data of PDMS material since it obtained not only low RSS but also no strain limit range. Sales et al. [14] studied mechanical characterization of PDMS with different mixing. The results for the tensile test showed that an increase in the amount of cure agent reduced the tensile strength. The hardness values obtained were 41.7±0.95, 43.2±1.03 and 37.2±1.14 Shore A for pure PDMS with ratios equal to 10:1ma, 10:2 and 10:3, respectively.

Many researchers have focused on formulating mathematical or finite element models of micropillar-like structures to investigate their mechanical behaviors under various load types. Rathod et al. [15] studied engineered ridge and micropillar array detectors to quantify the directional migration of fibroblasts. They converted the defections of a micropillar made of PDMS for various aspect ratios into forces using a finite element model in ABAQUS software based on neo-Hookean and Arruda-Boyce constitutive models. Differences in the measured forces arise due to the aspect ratio of the micropillars and the assumed material model used to define the constitutive properties of the pillar material. Pakawan et al. [16] studied the effect of PDMS substrate thickness on the mechanical behavior of PDMS micropillar patterns under compressive loading using the finite element method in the ANSYS Mechanical APDL software. The constitutive models consisted of Mooney-Rivlin (2, 3 and 5 parameters), Ogden (1^{st}, 2^{nd}, and 3^{rd} orders), Neo Hookean, Polynomial (1^{st} and 2^{nd} orders), Arruda-Boyce, Gent and Yeoh (1^{st}, 2^{nd}, and 3^{rd} orders) models were curved fitting with experiment data from uniaxial compression test. They found that the most accurate constitutive model was Mooney-Rivlin 5-parameter model for the low strain range. Since there was limitation of computation ability in extremely large FE model, the convergences of the FE results on the FE models of F3 micropattern was 84 micropillars. Furthermore, the micropillar without the substrate did not lateral collapse when subjected to compressive stress. As substrate thickness decreased, compressive strength declined, and elastic stiffness increased. Pakawan et al. [17] extended their work [16] to study the compressive behavior of micropillar patterns fabricated from PDMS material which had a rectangular cross-section and various micropillar's aspect ratios. They studied the finite element analyses of micropillar patterns in the ANSYS Mechanical APDL software and the Mooney-Rivlin 5 parameter model was used to model PDMS material under uniaxial compression. The convergences of the FE results were found on all micropillar patterns which were F3 micropattern (84 micropillars), F4 micropattern (84 micropillars), F8 micropattern (70 micropillars) and F13 micropattern (12 cells) on the 150 μm thick substrate. They found that the micropillar's compressive strength and elastic stiffness were unaffected by the aspect ratio of a micropillar. Moreover, the F13 micropattern has the lowest droplet contact angle, and the highest elastic stiffness and compressive strength. Cornec and Lilleodden [18] discovered new approach for determination of stress-strain curves from micropillar made from glass fused silica under compression and studied comprehensive numerical analysis for perfect and imperfect micropillars in finite element software ABAQUS. Marulli et al. [19] studied a finite element framework for the simulation of bio-inspired adhesives with mushroom-shaped microstructures. Kareem [20] proposed mathematical modeling of an electrostatic MEMS with tilted elastomeric micro-pillars. The model incorporates three coupled sets of nonlinear differential equations that govern the longitudinal and transverse vibrations of the PDMS pillars, as well as the transverse vibrations of the moving electrode.

This research was an extended work of Pakawan et al. [17] to investigate the accurate compressive behavior of micropillar patterns made of PDMS material. We also proposed a novel mathematical technique implemented in PP algorithm [13], called Modified PP algorithm. This technique aims to ascertain material constants and their associated stability regions. Finally, the accurate material model of PDMS and compressive behaviors of the micropillar patterns could be accomplished.

2. Theory

Thai Microelectronics Centre (TMEC) used soft lithography techniques to fabricate hydrophobic sheets made of PDMS material (having ratio of a PDMS monomer to a curing agent ratio of 10:1) for various micropillar patterns. F8 and F13 micropatterns had unique hydrophobic properties as shown in Figs. 1-2. The F13 pattern (called the sharklet pattern) has high compressive strength but low WCA of 134.7^{o}, while the F8 pattern has high WCA of 143.8^{o} but moderate compressive strength [17]. This research studied compressive behavior of micropillar patterns with an accurate constitutive material model as discussed in [13]. Here, we introduced the novel modified PP algorithm to determine accurate material constants from the Ogden 3^{rd} order model. Finally, these micropillar patterns were modelled and analysed in ANSYS Mechanical APDL 2019 R3 software.

2.1. Finite Element Models

For minimizing FE computational time and convergence of FE results, the replicas of micropillar patterns were studied as discussed in [16-17]. The FE models of F8 and F13 micropatterns consisting of 70 micropillars and 12 cells are shown in Figs. 3-4 respectively. Furthermore, all replicas of micropillar patterns were modeled on 150 μm thick substrate in which the substrates were long enough for studying only on interactions between micropillars as listed in Table 1-2. The FE models were constructed by the SOLID186 element which was the 20-nodes structural solid element which has 3 translations in the x, y, and z directions on each node. The number of elements of each FE models as listed in Table 1-2. The boundary conditions were that all nodes on the bottom surface were fixed in all degree of freedom while all nodes on the top surface were coupled with the displacement in the z-direction and moved downward to displacement of z = -20 μm. The surface-to-surface contact without friction was applied to each micropillar. The accurate constitutive model for PDMS material under uniaxial compression loading was Ogden 3^{rd} order model in which its material constants obtained from modified PP algorithm were illustrated in Table 3.

2.2. PDMS Material Models

The Ogden 3^{rd} order model accurately formulates the nonlinear deformation of a PDMS material [13]. Here, the

DOI:10.4186/ej.2024.28.6.25

stress-strain relation is derived from the strain energy density function (W).

2.2.1. Hyperelastic constitutive model

The Hyperelastic constitutive model is a constitutive equation of strain energy density function W which provides stress–strain relations for rubber-like materials.

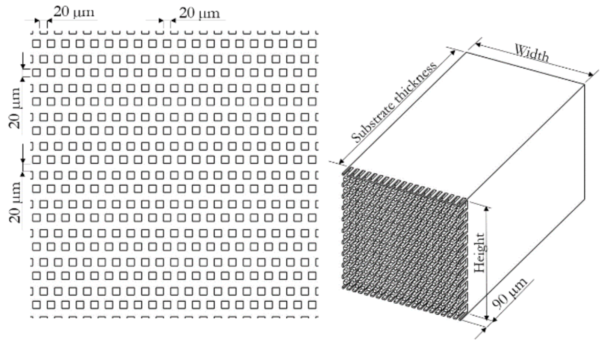

Fig. 1. Dimension of the F8 micropattern [17].

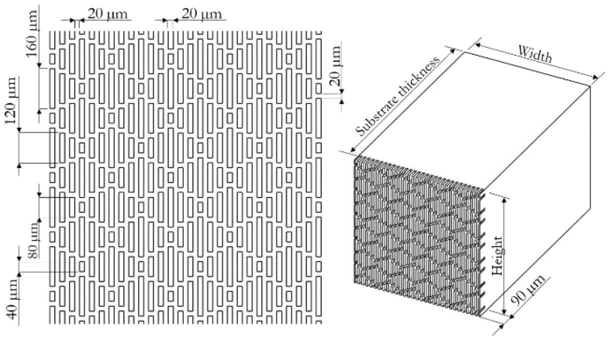

Fig. 2. Dimension of the F13 micropattern [17].

2.2.1.1. Ogden model

Ogden model is a general hyperelastic model in which its strain energy density is expressed in terms of the principal stretches. The strain energy density W can be written in Eq. (1).

$$W = \sum_{i=1}^{n} \frac{\mu_i}{\alpha_i} \left(\lambda_1^{\alpha_i} + \lambda_2^{\alpha_i} + \lambda_3^{\alpha_i} - 3 \right) \quad (1)$$

$$W = \sum_{i=1}^{n} \frac{\mu_i}{\alpha_i} \left(\lambda_1^{\alpha_i} + \lambda_2^{\alpha_i} + \lambda_3^{\alpha_i} - 3 \right)$$

where the stretch ratios λ_1, λ_2, and λ_3 obtain from elastomer material testing which composes of uniaxial test, equibiaxial test, and planar test; μ_i and α_i are material constants. For incompressible materials subjected uniaxial test, the three principal stretch ratios are given as $\lambda_1 = \lambda$, $\lambda_2 = \lambda^{-0.5}$, and $\lambda_3 = \lambda^{-0.5}$.

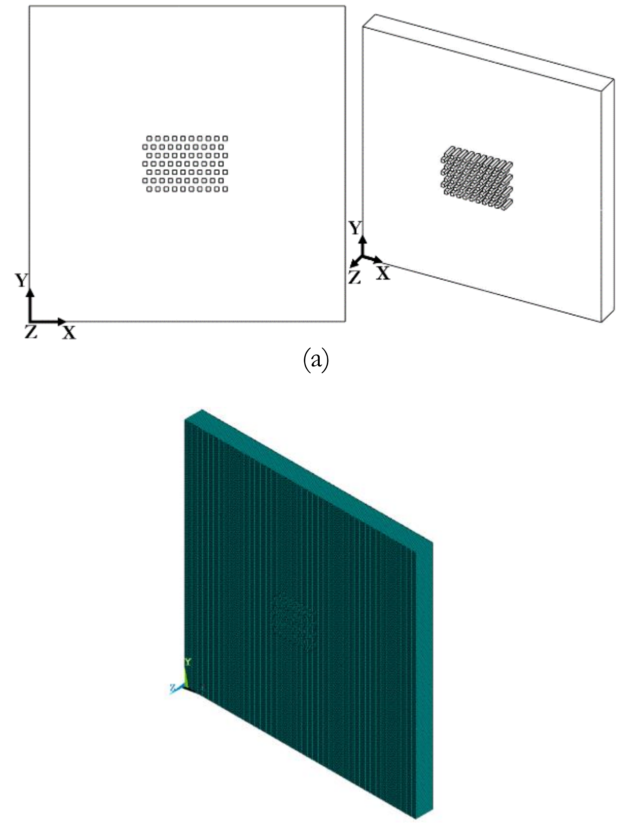

(a)

(b)

Fig. 3. (a) 3D models and (b) the FE model of F8 micropattern for 70 micropillars [13].

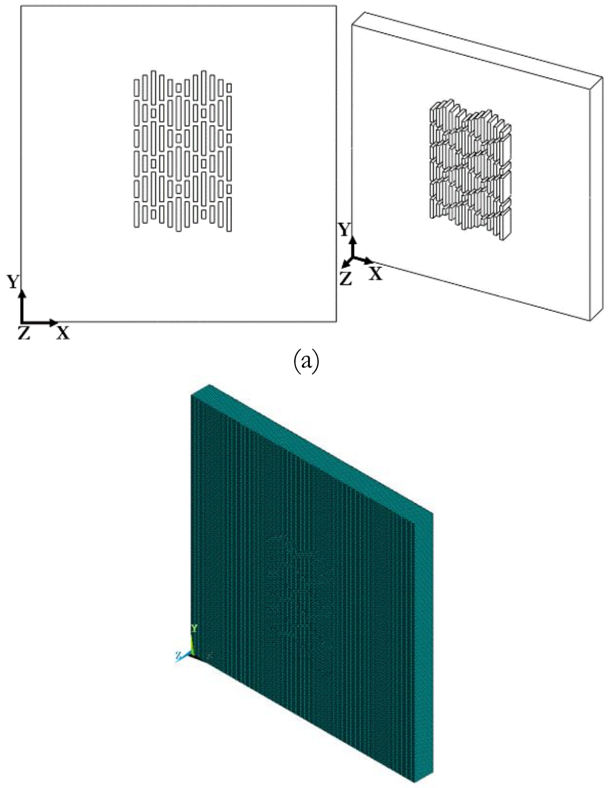

(a)

(b)

Fig. 4. (a) 3D models and (b) the FE model of F13 micropattern for 12 cells [13].

DOI:10.4186/ej.2024.28.6.25

Table 1. The number of elements of F8 micropattern.

Number of Micropillars	Number of elements	Width (μm) x Height (μm)
70	48,892	2,000 x 2,000

Table 2. FE models of F13 micropattern.

Number of Cells	Number of elements	Width (μm) x Height (μm)
12	59,400	1,800 x 1,800

2.2.1.2. Mooney-Rivlin model

Mooney-Rivlin model is developed from Neo-Hookean model. The strain energy density function. This model is generated from a linear combination of two invariants. This model is popular for modelling the large strain nonlinear behaviour of incompressible materials. The strain energy density *W* can be expressed in Eq. (2).

$$W = \sum_{i+j=1}^{n} C_{ij} \left(I_1 - 3\right)^i \left(I_2 - 3\right)^j \tag{2}$$

where strain invariants I_1 and I_2 can be written as

$$W = \sum_{i=1} \frac{\mu_i}{\alpha_i}\left(\lambda_1^{\alpha_i} + \lambda_2^{\alpha_i} + \lambda_3^{\alpha_i} - 3\right)$$

$$I_1 = \lambda^2 + \lambda^{-2} + 1 \tag{3}$$

$$I_2 = \lambda^2 + \lambda^{-2} + 1 \tag{4}$$

and C_{ij} are material constants.

2.2.2. Determination of stresses

An engineering stress can be derived from derivative of strain energy density function by stretch ratio as given in Eq. (14).

$$\sigma_i = \frac{\partial W}{\partial \lambda_i} \tag{5}$$

where σ_i and λ_i are an engineering stress and a stretch ratio in *i*-direction respectively.

2.2.3. Equivalent Von mises strain

Equivalent Von mises strain ε_e is a parameter used to monitor magnitude of strain in hyperelastic materials experiencing large deformation and can be written as

$$\varepsilon_e = \frac{1}{1+\nu'} \sqrt{\frac{1}{2}\begin{bmatrix} \left(\varepsilon_1 - \varepsilon_2\right)^2 + \left(\varepsilon_1 - \varepsilon_3\right)^2 \\ + \left(\varepsilon_2 - \varepsilon_3\right)^2 \end{bmatrix}} \tag{6}$$

where ν' is the effective Poisson's ratio which is generally considered as 0.5; ε_1, ε_2, and ε_3 are the principal strains.

2.2.4. Determination of stability regions

The stability region of each constitutive model can be determined from the Drucker stability condition for the first three modes of deformation. The condition requires that the changes of the true stress and true strain are satisfied in the inequality.

$$d\sigma : d\varepsilon > 0 \tag{7}$$

For isotropic hyperelastic materials, the inequality can be represented in terms of the principal stresses and strains as given in Eq. (8).

$$d\sigma_1 d\varepsilon_1 + d\sigma_2 d\varepsilon_2 + d\sigma_3 d\varepsilon_3 > 0 \tag{8}$$

For incompressible materials, we assigned $\sigma_3 = d\sigma_3 = 0$ into Eq. (8); therefore, the inequality is written as shown in Eq. (9).

$$d\sigma_1 d\varepsilon_1 + d\sigma_2 d\varepsilon_2 > 0 \tag{9}$$

where σ_i is the Cauchy stress in *i*-principal direction and ε_i is Cauchy strain in *i*-principal direction. The changes of true strain are related to the stretch ratios which can be given in Eq. (10).

$$d\varepsilon_i = \frac{d\lambda_i}{\lambda_i} \tag{10}$$

The relation between the changes of the Cauchy stress and the Cauchy strain can be formulated by the matrix equation as written in Eq. (11).

$$\begin{Bmatrix} d\sigma_1 \\ d\sigma_2 \end{Bmatrix} = \left[D\right] \begin{Bmatrix} d\varepsilon_1 \\ d\varepsilon_2 \end{Bmatrix} \tag{11}$$

where D is the tangential stiffness matrix, and each element of D can be calculated from Eq. (12).

$$\left[D\right] = \begin{bmatrix} \lambda_1 \dfrac{d\sigma_1}{d\lambda_1} & \lambda_2 \dfrac{d\sigma_1}{d\lambda_2} \\ \lambda_1 \dfrac{d\sigma_2}{d\lambda_1} & \lambda_2 \dfrac{d\sigma_2}{d\lambda_2} \end{bmatrix} \tag{12}$$

2.3. Residual Sum of Squares

The residual sum of squares (RSS) used to measure an error between the constitutive hyperelastic models and the uniaxial data testing. Additionally, it is also used as an optimality criterion in parameter selection and model selection which can be calculated by Eq. (13).

$$RSS = \sum_{i=1}^{N} \left(\sigma_i - \sigma\right)^2 \tag{13}$$

where σ_i is the engineering stress obtained from experimental data, σ is the engineering stress obtained from hyperelastic constitutive models, and *N* is a numbers of data points.

3. Methodology

3.1. Determination of the Material Constants from Ogden 3rd Order Model

The material constants of Ogden 3rd order model are obtained from modified PP algorithm which is MATLAB code implemented in the previous PP algorithm as discussed in [13].

3.1.1. Data selection

The uniaxial experimental data obtained from [16] is smoothed by 6th order polynomial fitting after that the strain range T is equally divided by the number of strain intervals which gives the maximum interval length L_{max} written in Eq. (14).

$$L_{\max} = \frac{T}{n} \tag{14}$$

where

$$T = \varepsilon_{\max} - \varepsilon_{\min} \tag{15}$$

and n is number of material constants in constitutive models.

The uniaxial test data will be accurately matched and smoothed by polynomial functions as shown in Fig. 6. $\sigma_{Fit}^{\{i\}}$ and $\varepsilon_{Eng}^{\{i\}}$ are the fitted engineering stress and strain at the end of an i-interval respectively.

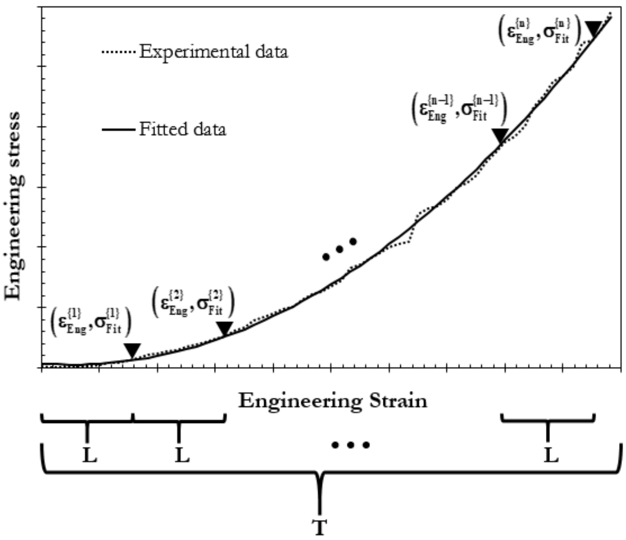

Fig. 6. Selection of the engineering stress-strain data [21].

Hyperelastic constitutive models are generally written in a function of stretch ratios, the stretch ratio at the end of i-interval can be expressed as shown in Eq. (16).

$$\lambda^{\{i\}} = 1 + \varepsilon_{Eng}^{\{i\}} \tag{16}$$

In Ogden model, material constants cannot be detached from a matrix of hyperelastic constitutive models; however, it can solve by substituting pairs of n^{th} data point in each row of Eq. (17).

$$\begin{bmatrix} \sum_{i=1}^{3} \mu_i \left(\left(\lambda^{\{1\}}\right)^{\alpha_i - 1} - \left(\lambda^{\{1\}}\right)^{-0.5\alpha_i - 1} \right) \\ \sum_{i=1}^{3} \mu_i \left(\left(\lambda^{\{2\}}\right)^{\alpha_i - 1} - \left(\lambda^{\{2\}}\right)^{-0.5\alpha_i - 1} \right) \\ \vdots \\ \sum_{i=1}^{3} \mu_i \left(\left(\lambda^{\{6\}}\right)^{\alpha_i - 1} - \left(\lambda^{\{6\}}\right)^{-0.5\alpha_i - 1} \right) \end{bmatrix} = \begin{bmatrix} \sigma_{Fit}^{\{1\}} \\ \sigma_{Fit}^{\{2\}} \\ \vdots \\ \sigma_{Fit}^{\{6\}} \end{bmatrix} \tag{17}$$

Ogden 3rd order model has 6 material constants which requires 6 selected data points at the ends of each interval length L, the material constants are determined from each component of stress vectors given in Eq. (18). Finally, material constants can then be solved by Levenberg–Marquardt algorithm [21] in MATLAB R2021a software for each value of L ($L \le L_{\max}$) such that the optimized material constants return the minimum RSS of stress-strain reproduction.

$$\begin{bmatrix} \left\{ \begin{matrix} \mu_1 \left(\left(\lambda^{\{1\}}\right)^{\alpha_1 - 1} - \left(\lambda^{\{1\}}\right)^{-0.5\alpha_1 - 1} \right) \\ + \mu_2 \left(\left(\lambda^{\{1\}}\right)^{\alpha_2 - 1} - \left(\lambda^{\{1\}}\right)^{-0.5\alpha_2 - 1} \right) \end{matrix} \right\} \\ \left\{ \begin{matrix} \mu_1 \left(\left(\lambda^{\{2\}}\right)^{\alpha_1 - 1} - \left(\lambda^{\{2\}}\right)^{-0.5\alpha_1 - 1} \right) \\ + \mu_2 \left(\left(\lambda^{\{2\}}\right)^{\alpha_2 - 1} - \left(\lambda^{\{2\}}\right)^{-0.5\alpha_2 - 1} \right) \end{matrix} \right\} \\ \left\{ \begin{matrix} \mu_1 \left(\left(\lambda^{\{3\}}\right)^{\alpha_1 - 1} - \left(\lambda^{\{3\}}\right)^{-0.5\alpha_1 - 1} \right) \\ + \mu_2 \left(\left(\lambda^{\{3\}}\right)^{\alpha_2 - 1} - \left(\lambda^{\{3\}}\right)^{-0.5\alpha_2 - 1} \right) \end{matrix} \right\} \\ \left\{ \begin{matrix} \mu_1 \left(\left(\lambda^{\{4\}}\right)^{\alpha_1 - 1} - \left(\lambda^{\{4\}}\right)^{-0.5\alpha_1 - 1} \right) \\ + \mu_2 \left(\left(\lambda^{\{4\}}\right)^{\alpha_2 - 1} - \left(\lambda^{\{4\}}\right)^{-0.5\alpha_2 - 1} \right) \end{matrix} \right\} \end{bmatrix} = \begin{bmatrix} \sigma_{Fit}^{\{1\}} \\ \sigma_{Fit}^{\{2\}} \\ \sigma_{Fit}^{\{3\}} \\ \sigma_{Fit}^{\{4\}} \end{bmatrix} \tag{18}$$

3.1.2. Determination of stability regions

Constitutive equation of Ogden model depends only on the stretch ratio; therefore, each element of the symmetric matrix D is determined from Eq. (19).

$$D = \begin{bmatrix} D_{11} & D_{12} \\ D_{21} & D_{22} \end{bmatrix} \tag{19}$$

where

$$D_{11} = \sum_{i=1}^{N} \left(\mu_i \alpha_i \lambda_1^{\alpha_i} + \mu_i \alpha_i \lambda_1^{-\alpha_i} \lambda_2^{-\alpha_i} \right)$$

$$D_{22} = \sum_{i=1}^{N} \left(\mu_i \alpha_i \lambda_2^{\alpha_i} + \mu_i \alpha_i \lambda_1^{-\alpha_i} \lambda_2^{-\alpha_i} \right)$$

$$D_{12} = D_{21} = \sum_{i=1}^{N} \left(\mu_i \alpha_i \lambda_1^{-\alpha_i} \lambda_2^{-\alpha_i} \right)$$

For material stability, the tangential stiffness matrix D must be positive definite which requires D to satisfied two conditions as written in Eqs. (20)-(21).

$$D_{11} + D_{22} > 0 \tag{20}$$

$$D_{11}D_{22} - D_{12}D_{21} > 0 \tag{21}$$

4. Results and Discussion

For uniaxial compressive test data of PDMS material obtained from [16], the material constants of Ogden 3rd model obtained from modified PP algorithm are compared with ones obtained from Ansys and PP algorithm is illustrated in Table 3 and their corresponding RSS are listed in Table 4. Figure 7 shows that the optimized L was 0.076 (compared to L_{max} = 0.082 in PP algorithm) which yielded RSS of 0.11569. We also found an increase in accuracy of reproduction of the stress-stress curve with modified PP algorithm because of these optimized L as shown in Fig. 8. Figure 9 shows the stress-strain curves reproduced from Mooney-Rivlin 5-parameter model (with Ansys) and Ogden 3rd order model (with Modified PP algorithm). Table 5 shows that Modified PP algorithm implemented for Ogden 3rd order model had the highest accuracy in reproduction of stress-strain curve. Moreover, these material constants have no strain limitation since left hand side terms of Eq. (20) and Eq. (21) are greater than zero as illustrated in Fig. 10.

Table 3. The material constants in Ogden 3rd order model determined from compressive test data of PDMS material.

Material constants	Ogden 3rd order model		
	ANSYS	PP	Modified PP
μ_1	4.36077	-0.07254	-0.08127
α_1	0.03681	-2.28350	-2.28604
μ_2	4.36085	-0.07255	-0.08130
α_2	0.03693	-2.28349	-2.28604
μ_3	4.36099	-0.10215	-0.08413
α_3	0.03688	-2.28322	-2.28653

Table 4. RSS between compressive test data and data reproduced from modified PP algorithm, *PP* algorithm, and ANSYS software with Ogden 3rd order Model.

	RSS
ANSYS	78.13855
PP algorithm	0.11570
Modified PP algorithm	0.11569

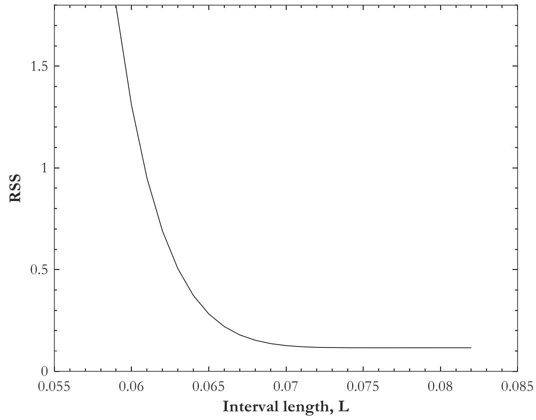

Fig. 7 The plot of interval length L vs. RSS.

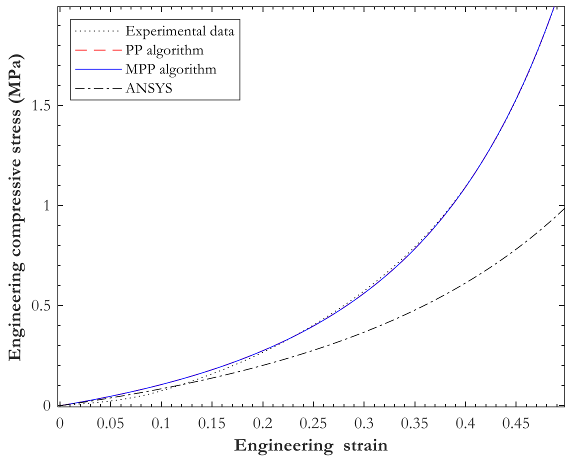

Fig. 8 Stress-strain curves reproduced from Ansys, PP algorithm and modified PP algorithm with Ogden 3rd order model compared to Experimental data.

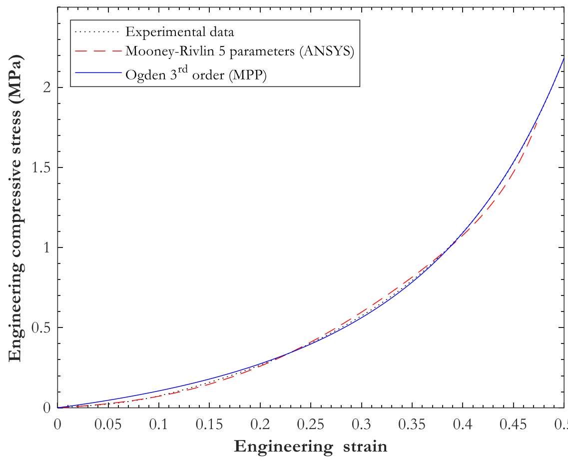

Fig. 9 Stress-strain curves reproducing from Ansys (with Mooney-Rivlin 5-parameter model) and modified PP algorithm (with Ogden 3rd order model) compared to Experimental data.

DOI:10.4186/ej.2024.28.6.25

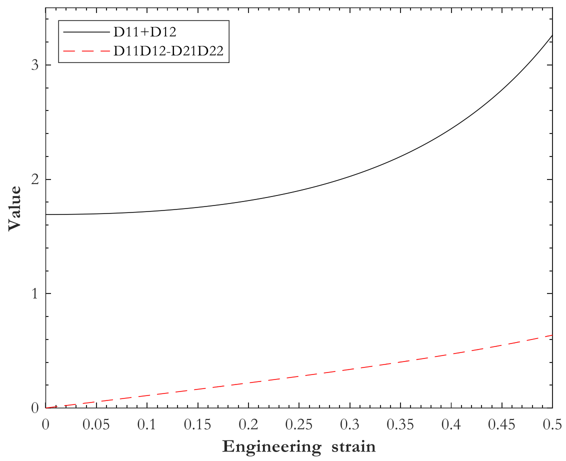

Fig. 10 Positive tangential stiffness for all strain range.

Table 5. RSS between uniaxial compressive test data and data reproduced from Ogden 3rd order model with modified PP algorithm and Mooney-Rivlin 5-parameter model with ANSYS.

Constitutive models	RSS
Mooney-Rivlin 5 parameters	0.12339
Ogden 3rd order	0.11569

Compressive behaviors of micropillar patterns subjected to compressive loading had been studied using Ogden 3rd order model and were compared to results studied by [17] as shown in Figs. 11-14. Figures 11-12 show the plot of uniform compressive loading and vertical displacement of F8 and F13 micropatterns respectively. We found quite different in load-deflection curves of micropatterns in which both F8 and F13 micropatterns are stiffer than results of [13]. Figures 13-14 show different collapse patterns compared to results of [13]. Figure 15-16 show the contour plot of various strains in F8 and F13 micropattern respectively. In our study, initial collapse micropillars occurred along the rim of micropatterns. The maximum von Mises strains were 0.374 and 0.096 for F8 and F13 respectively. The differ of our results may cause by no strain limit in our simulation compared to $\varepsilon_z \leq 0.225$ in [12-13]. Additionally, F8 and F13 micropatterns had sign of collapse of micropattern when compressive displacement of 17.715 μm and 4.817 μm respectively as discussed in [13]. Here, we found severe mesh distortion on some elements when the strain was relatively high which caused Ansys to terminate.

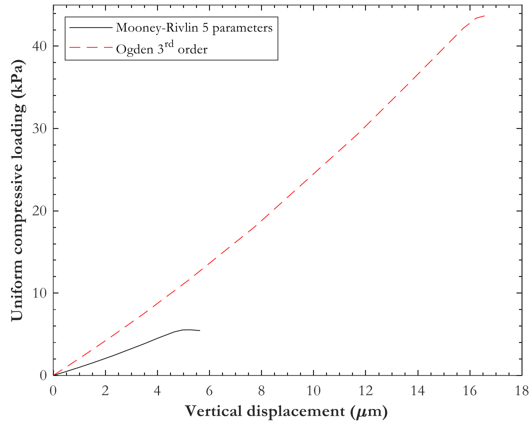

Fig. 11. Plot of uniform compressive loading and vertical displacement for F8 micropattern.

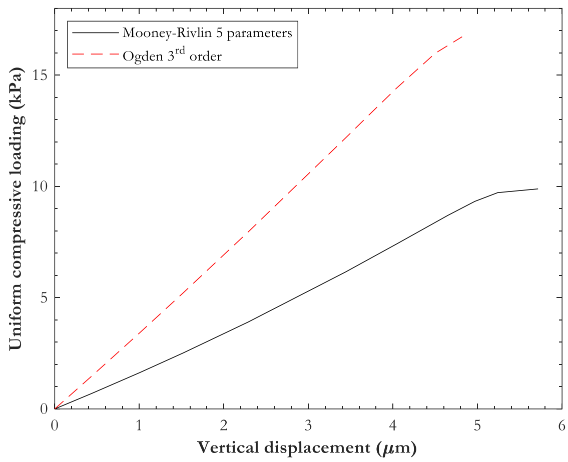

Fig. 12. Plot of compressive pressure and vertical displacement for F13 micropattern.

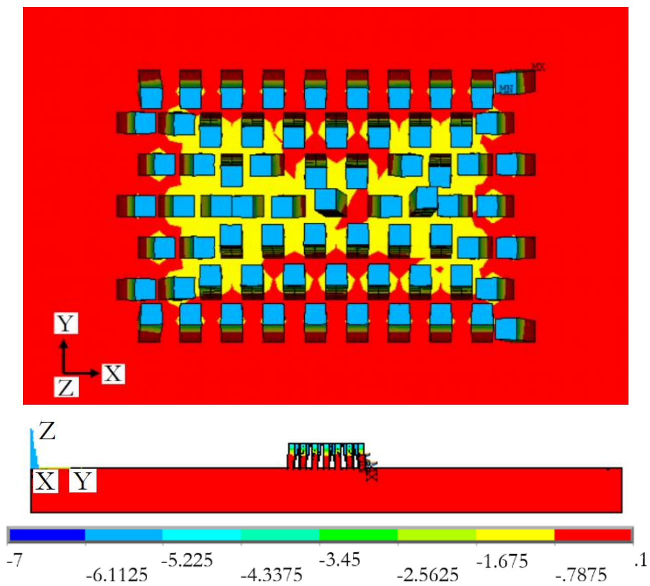

(a)

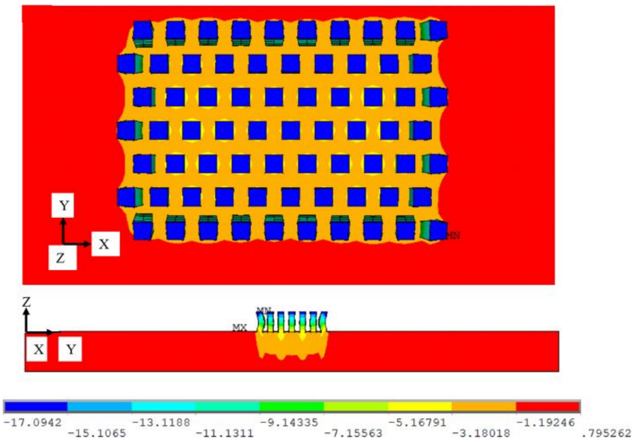

(b)

Fig. 13. Contour plot of deformation in the z-direction (unit in μm) of F8 micropattern at an initial collapse of micropillar patterns compared between (a) Mooney 5-parameter model [17]; (b) Ogden 3rd order model.

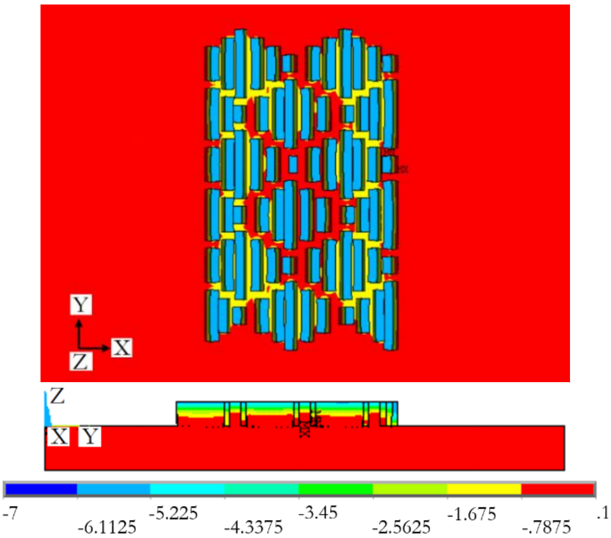

(a)

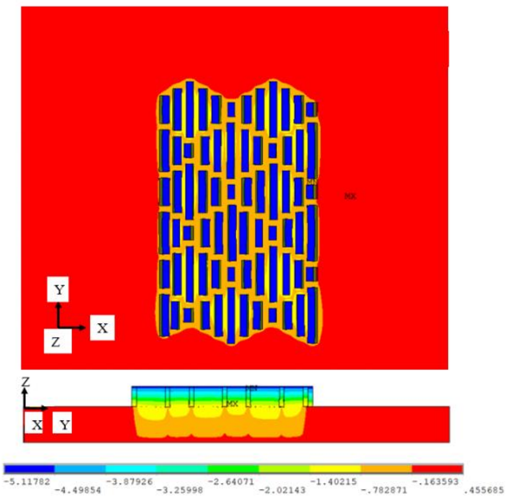

(b)

Fig. 14. Contour plot of deformation in the z-direction (unit in μm) of F13 micropattern at an initial collapse of micropatterns compared between (a) Mooney-Rivlin 5-parameter model [17], (b) Ogden 3rd order model.

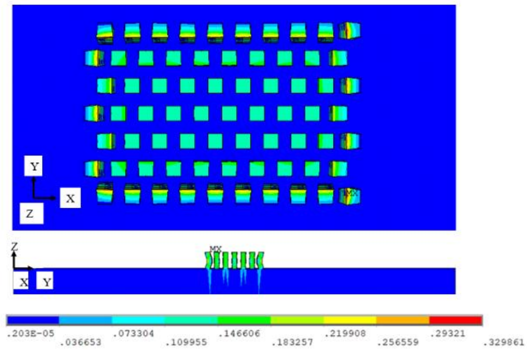

(a)

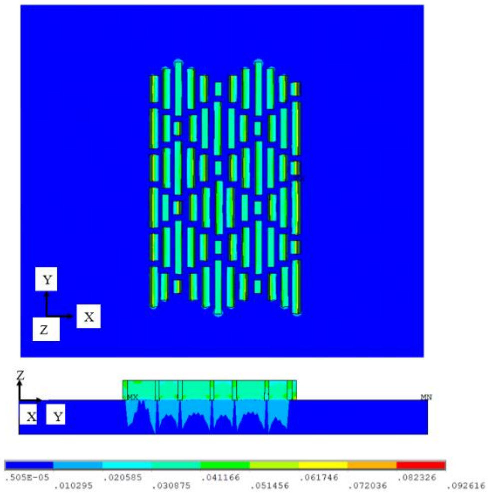

(b)

Fig. 15. Contour plot of Von Mises stress in MPa at an initial collapse of micropatterns for (a) F8 micropattern; (b) F13 micropattern.

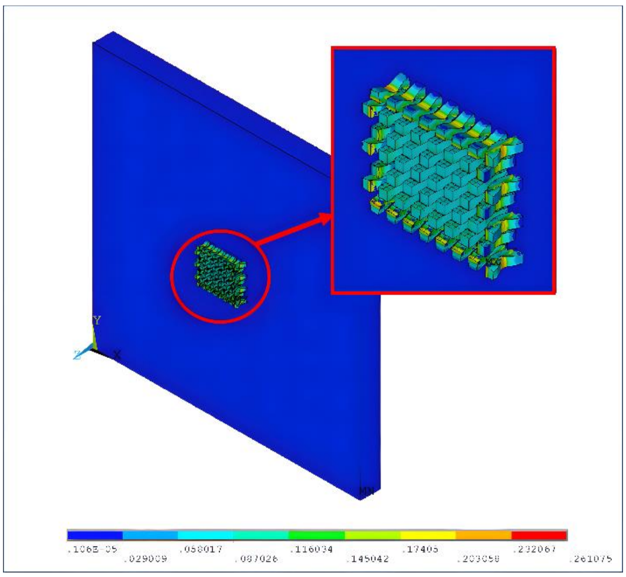

(a)

DOI:10.4186/ej.2024.28.6.25

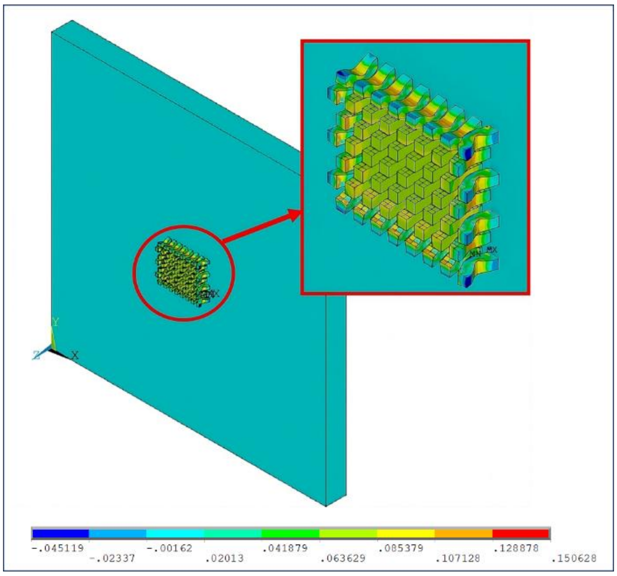

(b)

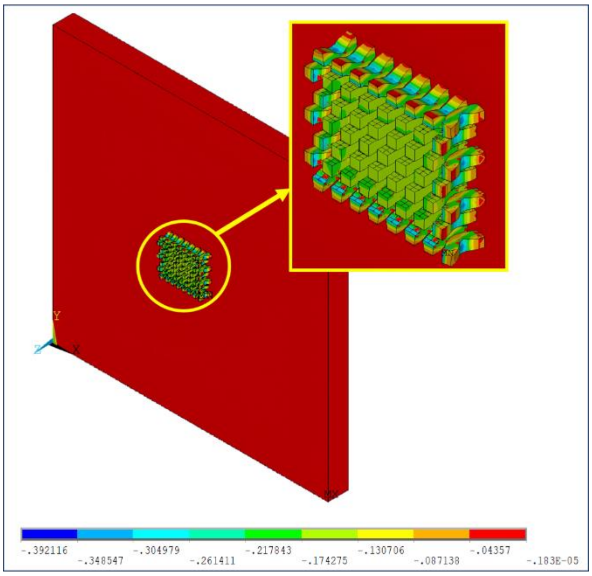

(c)

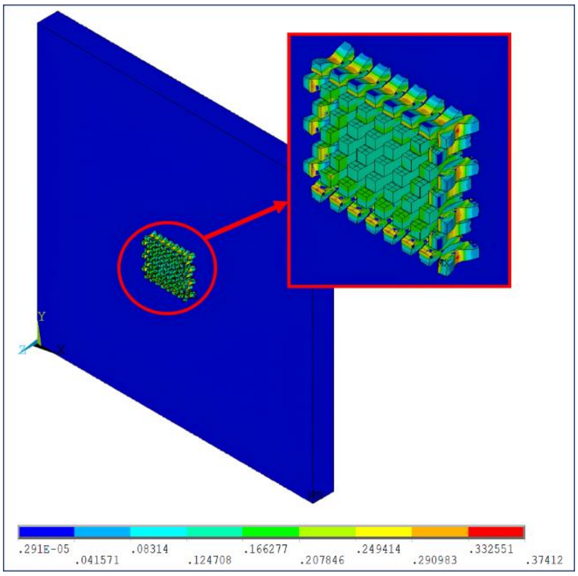

(d)

Fig. 16 Contour plot for various strain distributions on F8 micropattern at compressive displacement of 17.175 μm for (a) 1st Principal strain; (b) 2nd Principal strain; (c) 3rd Principal strain; (d) Equivalent Von Mises strain.

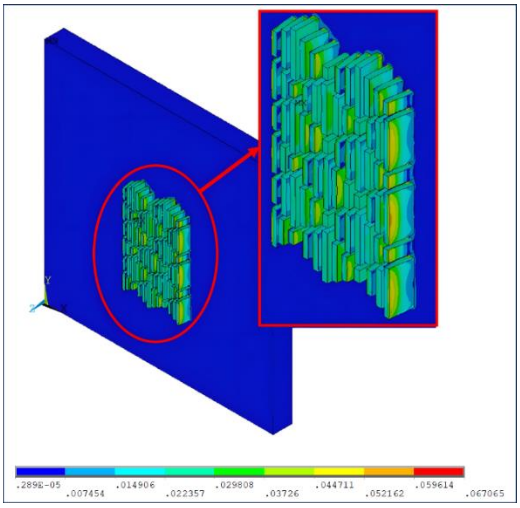

(a)

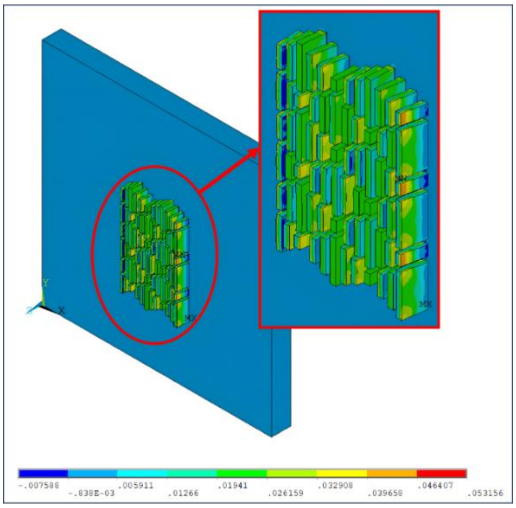

(b)

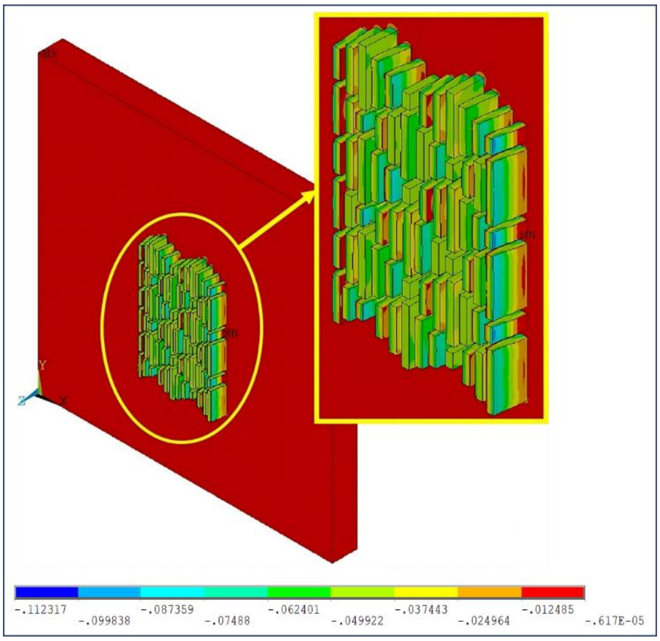

(c)

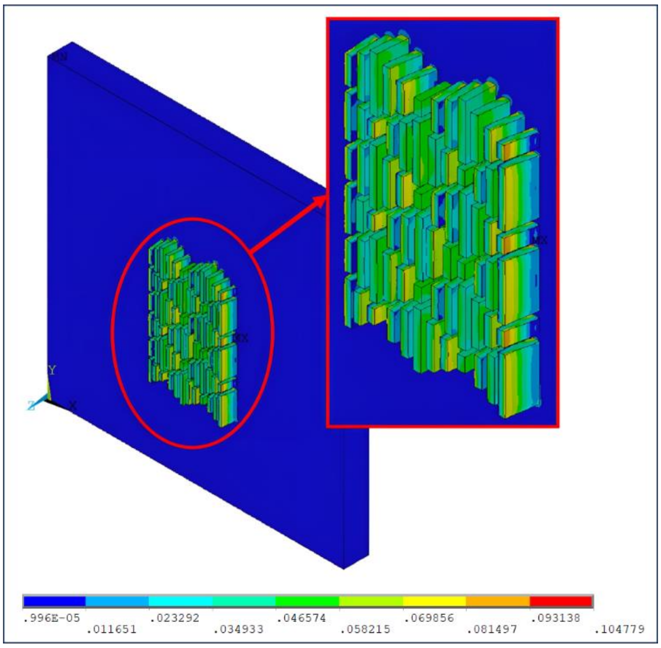

(d)

Figure. 17 Contour plot for various strain distributions on F13 micropattern at compressive displacement of 4.817 μm for (a) 1st Principal strain; (b) 2nd Principal strain; (c) 3rd Principal strain; (d) Equivalent Von Mises strain.

5. Conclusions

The compressive behaviors of micropillar patterns of F8 and F13 micropatterns had been studied with Ogden 3rd parameter model in Ansys APDL 2019R3 software. Moreover, we introduced a novel modified PP algorithm for determining material constants which is deemed innovative and intriguing in MATLAB 2021a software. This made the material constants more accurate than the study of [13] since we used the optimized strain interval length L instead of L_{max} as discussed in [13]. The load-deflection curves of micropillar patterns were stiffer than discussion in [17]. Moreover, the uniform compressive load P (in kPa) can be written as a function of vertical deformation z (in μm) as

$$P_{F8} = 3.5398z - 0.0791 \text{ for } 0 \le z \le 7.175\mu\text{m} \quad (22)$$

$$P_{F13} = 2.1081z - 0.801 \text{ for } 0 \le z \le 4.817\mu\text{m} \quad (23)$$

The R-squared for Eqs. (21-22) were 0.9971 and 0.9996 respectively. The maximum uniform compressive load, before initial collapse of micropatterns, were 34.334 kPa and 16.694 kPa for F8 and F13 micropatterns respectively.

Acknowledgement

The authors gratefully for Dr. Nithi Atthi, researcher at Thai Microelectronics Center (TMEC), for allowing us to use PDMS experimental data.

References

[1] Y. Liu and X. He and C. Yuan, P. Cao, and X. Bai, "Antifouling applications and fabrications of biomimetic microstructured surfaces: A review," *Journal of Advanced Research*, vol. 59, pp. 201-221, Oct. 2023.

[2] Y. Rahmawan, S. M. Kang, S. Y. Lee, K. Suh, and S. Yang, "Enhanced shear adhesion by mechanical interlocking of dual-scaled elastomeric micropillars with embedded silica particles," *Macromolecular Reaction Engineering*, vol. 7, no. 10, pp. 616-623, 2013.

[3] Y. Kim, Y. Chung, A. Tsao, and R. Maboudian, "Tuning micropillar tapering for optimal friction performance of thermoplastic gecko-inspired adhesive," *ACS Applied Materials & Interfaces*, vol. 6 no. 9, pp. 6936-6943, May 2014.

[4] A. M. A. Mohamed, A. M. Abdullah, and N. A. Younan, "Corrosion behavior of superhydrophobic surfaces: A review," *Arabian Journal of Chemistry*, vol. 8, no. 6, pp. 749-765, Nov. 2015.

[5] N. E. Oyunbaatar, D. H. Lee, S. J. Patil, E. S. Kim, and D. W. Lee, "Biomechanical characterization of cardiomyocyte using PDMS pillar with microgrooves," *Sensors*, vol. 16, pp. 1258-1270, Aug. 2016.

[6] A. Sabbah, A. Youssef, and P. Damman, "Superhydrophobic surfaces created by elastic instability of PDMS," *Appl. Sci.*, vol. 6, pp. 152-159, May 2016.

[7] N. Atthi, W. Sripumkhai, P. Pattamang, O. Thongsook, A. Srihapat, R. Meananeatra, J. Supadech, N. Klunngien, and W. Jeamsaksiri, "Fabrication of robust PDMS micro-structure with hydrophobic and antifouling properties," *Microelectronic Engineering*, vol. 224, p. 111255, Feb. 2020.

[8] M. Li, W. Luo, Y. Chen, Y. Zheng, and X. Cheng, "Fabrication and nanoindentation characterization of nickel micro-pillar mold for nanoimprint lithography," *Microelectronic Engineering*, vol. 250, p. 111636, Oct. 2021.

[9] H. T. Kim, and O. C. Jeong. "Measurement of nonlinear mechanical properties of surfactant-added poly (dimethylsiloxane)," *Jpn. J. Appl. Phys.*, vol. 51, no. 6S, p. 06FK07, Jun 2012.

[10] M. Shahzad, A. Kamran, M. Z. Siddiqui, and M. Farhan, "Mechanical characterization and FE modelling of a hyperelastic material," *Mat. Res.*, vol. 18, no. 5, pp. 918-924, Oct. 2015.

[11] J. E. Ribeiro, H. Lopes, P. Martins, and M. T. Braz-César. "Mechanical analysis of PDMS material using biaxial test," *AIMS Materials Science*, vol. 6, no. 1, pp. 97-110, Feb. 2019.

[12] K. Thanakhun and T. Puttapitukporn, "PDMS material models for anti-fouling surfaces using finite element method," *Eng. J.*, vol. 23, no. 6, pp. 381-398, Nov. 2019.

[13] J. Phothiphatcha and T. Puttapitukporn, "Determination of material parameters of PDMS material models by MATLAB," *Eng. J.*, vol. 25, no. 4, pp. 11-28, April 2021.

[14] Flaminio C. P. Sales, R. M. Ariati, V. T. Noronha, and J. E. Ribeiro, "Mechanical characterization of PDMS with different mixing," *Procedia Structural Integrity*, vol. 37, pp. 383–388, Jan. 2022.

[15] M. L. Rathod, N. Pareek, S. Agrawal, S. Jaddivada, D. W. Lee, and N. Gundiah, "Engineered ridge and micropillar array detectors to quantify the directional migration of fibroblasts," *RSC Advances*, vol. 7, no. 18, pp. 51436-51443, Oct. 2017.

[16] T. Pakawan, T. Puttapitukporn, N. Atthi, W. Sripumkhai, P. Pattamang, N. Klunngien, and W. Jeamsaksiri, "Compressive behaviors of micropillar sheets made of PDMS material using the finite element method," *Eng. J.*, vol. 24, no. 4, pp. 73-84, Jul. 2020.

[17] T. Pakawan, T. Puttapitukporn, N. Atthi, W. Sripumkhai, P. Pattamang, N. Klunngien, and W. Jeamsaksiri, "Compressive behaviors of micropillar patterns made of PDMS material using the finite element method," *Eng. J.*, vol. 25, no. 1, pp. 69-80, Jan. 2021.

[18] A. Cornec and E. Lilleodden, "Numerical analysis of micropillar compression behaviour and stress-strain curve estimation verified on glass fused silica," *Materials Today Communications*, vol. 33, p. 104971, Dec. 2022.

[19] M. R. Marulli, L. Heepe, S. N. Gorb, and M. Paggi, "A finite element framework for the simulation of bio-inspired adhesives with mushroom-shaped microstructures," *Mechanics Research Communications*, vol. 125, p. 103963, Aug. 2022

[20] A. H. Kareem, M. Fathalilou, and G. Rezazadeh, "Mathematical modeling of an electrostatic MEMS with tilted elastomeric micro-pillars," *Applied Mathematical Modelling*, vol. 131, pp. 306-322, Apr. 2024.

[21] A. Ranganathan, Ananth, "The Levenberg-Marquardt algorithm," *Tutorial on LM algorithm*, vol. 11, no. 1, pp. 101-110, Jun. 2004.

Tumrong Puttapitukporn received the B.Eng. degree in Mechanical Engineering from Kasetsart University, Thailang in 1998, and the M.S. and Ph.D. degree in Mechanical Engineering from Oregon State University, USA in 1999 and 2003 repectively.
He is currently the Associate Professor in Department of Mechanical Engineering, Kasetsat university, Thailand. His researach focus on finite element modeling and applications of generalized continuum theories.

Parawat Songpunnateegul received the B.Eng. degree in mechanical engineering from Kasetsart University, Thailand in 2019.